

# Enhanced electron coherence in atomically thin Nb<sub>3</sub>SiTe<sub>6</sub>

J. Hu<sup>1</sup>, X. Liu<sup>1</sup>, C. L. Yue<sup>1</sup>, J. Y. Liu<sup>1</sup>, H. W. Zhu<sup>1</sup>, J. B. He<sup>2</sup>, J. Wei<sup>1\*</sup>, Z. Q. Mao<sup>1\*</sup>, L. Yu. Antipina<sup>3,4,5</sup>, Z. I. Popov<sup>6</sup>, P. B. Sorokin<sup>3,4,5,7</sup>, T. J. Liu<sup>8</sup>, P. W. Adams<sup>8</sup>, S. M. A. Radmanesh<sup>9</sup>, L. Spinu<sup>9</sup>, H. Ji<sup>10</sup> and D. Natelson<sup>10</sup>

**It is now well established that many of the technologically important properties of two-dimensional (2D) materials, such as the extremely high carrier mobility in graphene<sup>1</sup> and the large direct band gaps in MoS<sub>2</sub> monolayers<sup>2</sup>, arise from quantum confinement. However, the influence of reduced dimensions on electron–phonon (e–ph) coupling and its attendant dephasing effects in such systems has remained unclear. Although phonon confinement<sup>3–7</sup> is expected to produce a suppression of e–ph interactions in 2D systems with rigid boundary conditions<sup>6,7</sup>, experimental verification of this has remained elusive<sup>8</sup>. Here, we show that the e–ph interaction is, indeed, modified by a phonon dimensionality crossover in layered Nb<sub>3</sub>SiTe<sub>6</sub> atomic crystals. When the thickness of the Nb<sub>3</sub>SiTe<sub>6</sub> crystals is reduced below a few unit cells, we observe an unexpected enhancement of the weak-antilocalization signature in magnetotransport. This finding strongly supports the theoretically predicted suppression of e–ph interactions caused by quantum confinement of phonons.**

Electron–phonon (e–ph) interactions in reduced dimensions have attracted wide interest for decades<sup>8,9</sup>. Confinement quantization of the phonon spectra<sup>10,11</sup> has been predicted to enhance e–ph interactions in free-standing 2D films<sup>3–6</sup>. In contrast, a gap is expected to open in the phonon spectra of films supported by a rigid boundary. This gap should reduce the e–ph interaction strength<sup>6,7</sup>. However, previous experimental studies have not provided a clear picture of the role of dimensionality in e–ph coupling. Early electron heating experiments found that the electron energy relaxation via phonon emission in reduced dimensions could not be described using bulk phonon theory<sup>12–14</sup>, suggesting that phonon dimensionality modifies the e–ph interaction. Enhanced e–ph scattering was reported in the 3D to 2D crossover regime in freestanding SiN<sub>x</sub> membranes<sup>15</sup>. However, similar studies using both freestanding and supported CuCr films suggested that the quantization of the phonon spectra has little effect on e–ph interaction<sup>16</sup>.

The e–ph interaction can also be probed by magnetotransport measurements in materials exhibiting weak antilocalization (WAL)—a correction to conductivity due to the destructive interference of backscattered partial electron waves. Given that such quantum interference is sensitive to the conduction electron phase coherence, which is generally limited by inelastic electron–electron

(e–e) and e–ph scattering at liquid helium temperatures<sup>8,17,18</sup>, WAL provides a measure of the e–ph scattering rate. Previous WAL studies on thermally evaporated metal wires/thin films suggested that the inelastic e–ph scattering rate is, in fact, insensitive to the phonon dimensionality<sup>19–21</sup>.

These conflicting experimental results and their inconsistency with theoretical predictions may be associated with the nature of the polycrystalline materials used in those studies, given the e–ph interaction has been predicted to also depend on electron's mean free path<sup>22–24</sup>. Therefore, single-crystalline nanostructured materials, which have minimal grain boundary scattering, should be much better suited for e–ph investigations. Recent advances in micro-exfoliation techniques<sup>1</sup> have made it possible to produce 2D single crystals that were previously inaccessible to the community. In this work, we report the observation of the WAL signature in a new ternary 2D system—Nb<sub>3</sub>SiTe<sub>6</sub> few-layer crystals. Through the study of the thickness dependence of WAL, we have observed clear evidence for the long-predicted suppression of e–ph interactions caused by 2D confinement of phonons<sup>6</sup>.

Nb<sub>3</sub>SiTe<sub>6</sub> was discovered two decades ago<sup>25</sup> but has scarcely been studied. As shown in Fig. 1a, Nb<sub>3</sub>SiTe<sub>6</sub> is a van der Waals material formed from stacks of Te–(Nb,Si)–Te sandwich layers. Each layer is composed of NbTe<sub>6</sub> prisms with Si ions inserted into the interstitial sites among these prisms (see detailed structure characteristics in Methods). Single crystals of Nb<sub>3</sub>SiTe<sub>6</sub> with lateral dimensions of a few millimetres (Fig. 1b, inset) were grown by chemical vapour transport. Excellent crystallinity is demonstrated by the sharp (0k0) X-ray diffraction peaks (Fig. 1b). Consistent with the layered structure, our resistivity measurements on bulk samples along in-plane ( $\rho_{\parallel}$ ) and out-of-plane ( $\rho_{\perp}$ ) directions, as shown in Fig. 1c, indicate that Nb<sub>3</sub>SiTe<sub>6</sub> is an anisotropic metal, with an anisotropic ratio  $\rho_{\perp}/\rho_{\parallel}$  increasing from 9 at 300 K to 22.5 at 2 K (Fig. 1c, top left inset). As revealed by the band structure calculations detailed in the Supplementary Information, such metallicity originates from the specific bonding state of Nb ions.

The micaceous nature of Nb<sub>3</sub>SiTe<sub>6</sub> allows it to be thinned down to atomically thin 2D crystals using micro-exfoliation<sup>1</sup>. Layers of ~3–5 nm in thickness can be easily produced, and even flakes as thin as only one unit cell (bilayer) are accessible, as illustrated by the micrograph of a large (>10  $\mu\text{m}$ ) bilayer flake in Fig. 1d,e. The quality and stability of the atomically thin Nb<sub>3</sub>SiTe<sub>6</sub> single-crystal

<sup>1</sup>Department of Physics and Engineering Physics, Tulane University, New Orleans, Louisiana 70118, USA. <sup>2</sup>Coordinated Instrument Facility, Tulane University, New Orleans, Louisiana 70118, USA. <sup>3</sup>Technological Institute for Superhard and Novel Carbon Materials, Troitsk, Moscow 142190, Russian Federation. <sup>4</sup>Moscow Institute of Physics and Technology, Moscow 141700, Russian Federation. <sup>5</sup>Emanuel Institute of Biochemical Physics, Moscow 119334, Russian Federation. <sup>6</sup>Kirensky Institute of Physics, Akademgorodok, Krasnoyarsk 660036, Russian Federation. <sup>7</sup>National University of Science and Technology MISiS, Moscow 119049, Russian Federation. <sup>8</sup>Department of Physics and Astronomy, Louisiana State University, Baton Rouge, Louisiana 70803, USA. <sup>9</sup>Advanced Materials Research Institute and Department of Physics, University of New Orleans, New Orleans, Louisiana 70148, USA. <sup>10</sup>Department of Physics and Astronomy, Rice University, Houston, Texas 77005, USA. \*e-mail: jwei1@tulane.edu; zmao@tulane.edu

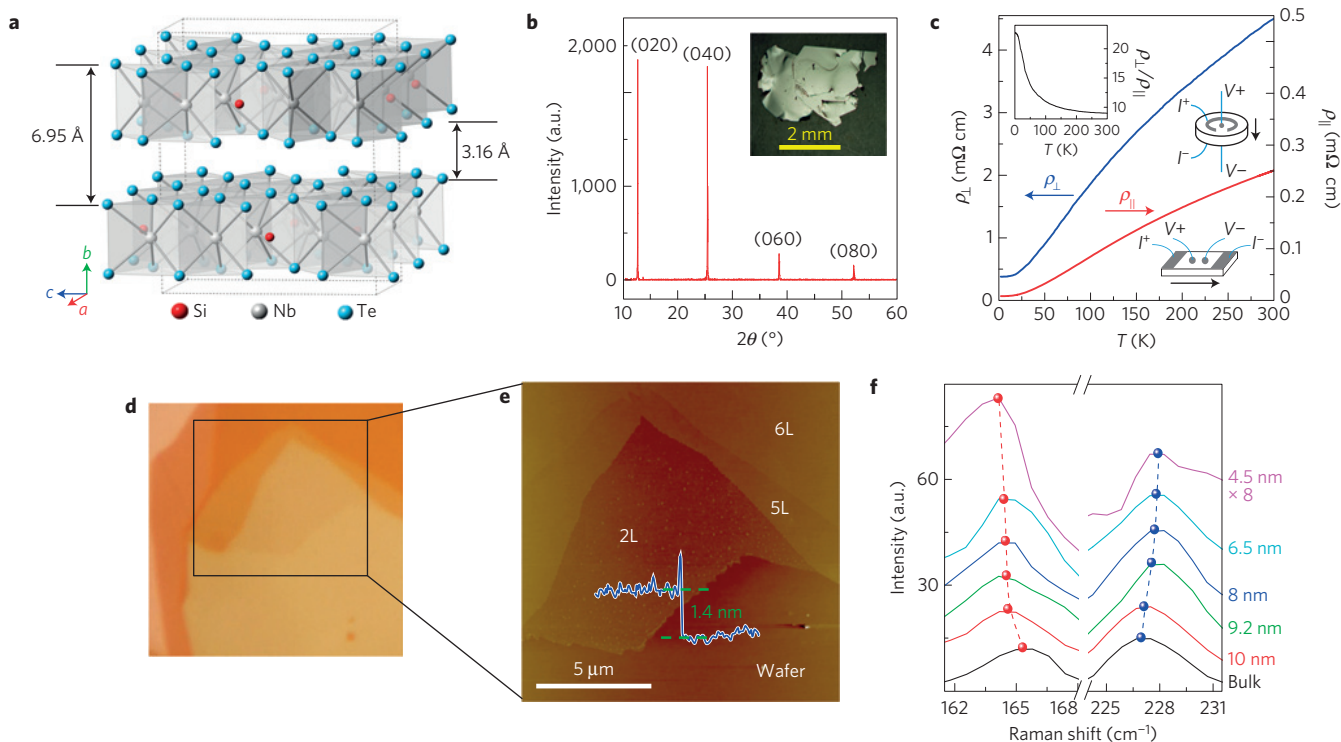


**Figure 1 | Characterization of bulk and thin-layer  $\text{Nb}_3\text{SiTe}_6$ .** **a**, Crystal structure of  $\text{Nb}_3\text{SiTe}_6$ . **b**, Single-crystal X-ray diffraction pattern along the  $(0k0)$  plane for bulk  $\text{Nb}_3\text{SiTe}_6$ . The out-of-plane lattice constant  $b$  is determined to be  $\sim 1.4$  nm, consistent with the previously reported structure with  $b = 1.3938(5)$  nm (ref. 25). Inset: optical image of a bulk  $\text{Nb}_3\text{SiTe}_6$  single crystal. **c**, Temperature dependences of the in-plane ( $\rho_{\parallel}$ ) and out-of-plane ( $\rho_{\perp}$ ) resistivity for the bulk  $\text{Nb}_3\text{SiTe}_6$  single crystals. Top left inset: anisotropic ratio ( $\rho_{\perp}/\rho_{\parallel}$ ) as a function of temperature. Right insets: contact lead configurations for  $\rho_{\perp}$  (upper) and  $\rho_{\parallel}$  (lower) measurements. **d**, Optical image of a  $\text{Nb}_3\text{SiTe}_6$  thin crystal. **e**, Atomic force microscopy image of a selected area from **d** with 2L, 5L and 6L representing bilayer, five-layer and six-layer, respectively. The inset shows the height of the bilayer ( $\sim 1.4$  nm) determined from the profile scan. **f**, Thickness dependence of Raman modes at 165 and 225  $\text{cm}^{-1}$  for  $\text{Nb}_3\text{SiTe}_6$  thin crystals (displaced vertically). The spectrum for the 4.5 nm flake is multiplied by a factor of eight. Full Raman spectra are given in the Supplementary Information.

flakes were demonstrated by TEM observations (see Methods). We further characterized the single-crystal flakes through Raman spectra measurements, and observed noticeable red- and blueshifts caused by the decrease in thickness for 165 and 225  $\text{cm}^{-1}$  modes, respectively (Fig. 1f). Often, such Raman mode shifts reflect variations of phonon spectra with reducing dimensionality, as seen in transition metal dichalcogenides such as  $\text{MoS}_2$  (ref. 26).

We have fabricated  $\text{Nb}_3\text{SiTe}_6$  electronic nano-devices using standard electron-beam lithography. Although we are able to thin  $\text{Nb}_3\text{SiTe}_6$  crystals down to one unit cell, successful devices with good electrical contacts can be prepared only on flakes with thicknesses  $t \geq 6$  nm. Overall, we observed a systematic increase of resistivity with decreasing thickness (Fig. 2a), which should be due to the enhanced importance of interfacial scattering in thinner samples. For relatively thick flakes ( $> 12$  nm), the temperature dependence of the resistivity is very similar to that of the bulk sample. However, when the thickness is decreased below 12 nm, marked changes emerge in the temperature dependence of the resistivity. These thinner samples develop a low-temperature upturn in the resistivity that is more pronounced with decreasing thickness. As discussed in the Supplementary Information, these resistivity upturns follow a  $\log(T)$  dependence, suggesting that they are due to 2D electron–electron interactions (EEI; refs 18,27) which become more pronounced with reducing sample thickness<sup>18</sup>. Other possible mechanisms accounting for the low-temperature upturn in resistivity, such as the Kondo effect<sup>28</sup> and weak localization<sup>8,17,18</sup>, which are associated with negative magnetoresistance (MR), can be ruled out by the observation of positive MR in all our  $\text{Nb}_3\text{SiTe}_6$  thin crystals (Fig. 2b,c).

Interestingly, although thick flakes (for example,  $t = 30$  nm and above) show a classical  $B^2$  dependence in MR, with decreasing flake thickness, the field dependence of MR evolves to sub-linear behaviour with a zero-field dip gradually developing below  $t = 15$  nm (Fig. 2b). Zero-field MR dips are known to originate from WAL in systems with strong spin–orbit coupling (SOC; refs 8,17,18), but they can also arise from Zeeman splitting of the EEI correction to the density of states in a disordered conductor<sup>18,27</sup>. However, EEI is insensitive to low magnetic fields owing to its large characteristic fields<sup>18</sup>, whereas WAL is a low-field phenomenon<sup>8,17,18</sup>. Furthermore, these two mechanisms can be distinguished by measurements of the angular dependence of magnetoresistance (AMR). The EEI correction to conductance is not sensitive to the magnetic field orientation<sup>27</sup>, whereas WAL is<sup>18</sup> (see the detailed discussions in Methods). Our AMR data rules out EEI as the origin of the zero-field MR dip, but they are consistent with WAL. As seen in Fig. 2d, when the applied field is high (for example, 9 and 3 T), the rotation of the field in the  $x$ – $z$  plane (see the inset to Fig. 2d) leads to a  $\cos^2\theta$  dependence of AMR, indicating the orbital MR ( $\propto B_z^2 = B^2 \cos^2\theta$ ) dominates at high field. In the low-field regime, the  $\cos^2\theta$  dependence disappears, indicating that classical MR can be neglected. However, in this regime, the AMR data shows a striking dip when the field is oriented parallel to the probe current, and becomes almost constant when the orientation angle of the field is beyond a critical value, as indicated by the arrows in Fig. 2d. This anisotropic AMR reflects the expected suppression of WAL by the perpendicular component of the magnetic field.

The observation of WAL in  $\text{Nb}_3\text{SiTe}_6$  is not surprising owing to relatively strong SOC induced by the heavy elements Nb and

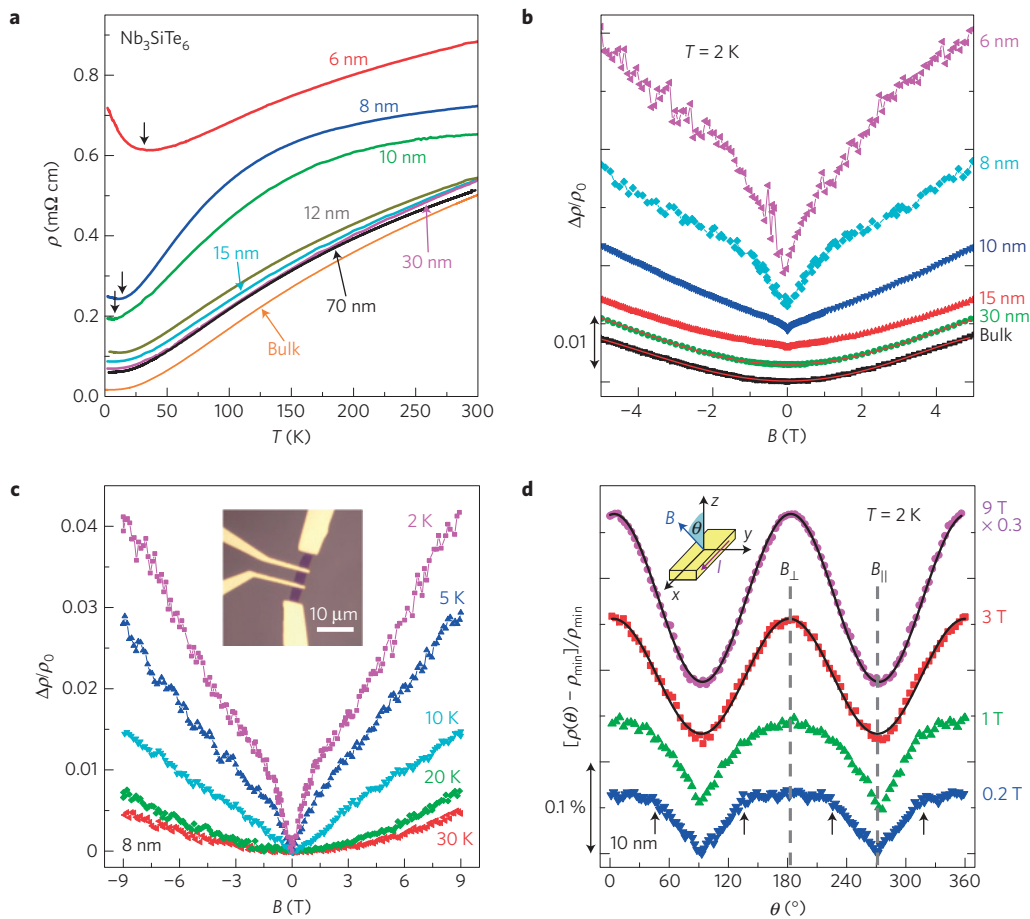


**Figure 2 | Transport properties of Nb<sub>3</sub>SiTe<sub>6</sub> nano-devices.** **a**, Temperature dependence of resistivity of Nb<sub>3</sub>SiTe<sub>6</sub> thin-flake crystals with various thicknesses. The bulk resistivity data is adopted from Fig. 1c for comparison. The downward arrows mark the resistivity upturns. **b**, Normalized magnetoresistivity  $\Delta\rho/\rho_0 = [\rho(B) - \rho(B=0)]/\rho(B=0)$ , at  $T = 2$  K for Nb<sub>3</sub>SiTe<sub>6</sub> crystals of various thicknesses. Data for different thickness are displaced vertically for clarity. Fits of MR to  $B^2$  (solid lines) are shown for the 30 nm thin crystal and the bulk sample. **c**, Normalized magnetoresistivity,  $\Delta\rho/\rho_0$  of a 8 nm Nb<sub>3</sub>SiTe<sub>6</sub> flake at various temperatures. The inset shows the optical image of this device. The magnetic field was applied along the out-of-plane direction. **d**, Isothermal angular magnetoresistance (AMR)  $\Delta\rho/\rho_{\min} = [\rho(\theta) - \rho_{\min}]/\rho_{\min}$  at  $T = 2$  K under various magnetic fields for the 10 nm device.  $\rho_{\min}$  is the resistance minimum, which occurs when the field,  $B$ , is oriented parallel to the probe current,  $I$  (indicated by  $B_{\parallel}$ ). The angle  $\theta$  is the angle between the out-of-plane axis ( $z$ -axis) and the magnetic field vector.  $B_{\perp}$  and  $B_{\parallel}$  defines the position where field is perpendicular and parallel to the current direction, respectively. The value of the AMR at 9 T is multiplied by a factor of 0.3. The solid lines show fits of the 9 T and 3 T data to the  $\cos^2\theta$  dependence. Inset: schematic of the measurement set-up. The magnetic field rotates within the  $x$ - $z$  plane defined by the current ( $x$ -axis) and out-of-plane axis ( $z$ -axis).

**Table 1 | Parameters of e-e and e-ph interactions obtained from fits of the temperature dependence of  $\tau_{\phi}^{-1}$ .**

	$\tau_0^{-1}$ (s <sup>-1</sup> )	$A$ (s <sup>-1</sup> K <sup>-<math>P_e</math></sup> )	$B$ (s <sup>-1</sup> K <sup>-<math>P_{ph}</math></sup> )	$P_e$	$P_{ph}$
8 nm	$5.0(\pm 0.2) \times 10^{11}$	$1.3(\pm 0.2) \times 10^{11}$	$4.1(\pm 0.3) \times 10^6$	$0.95(\pm 0.05)$	$3.63(\pm 0.20)$
10 nm	$4.6(\pm 0.1) \times 10^{11}$	$1.7(\pm 0.3) \times 10^{11}$	$1.3(\pm 0.2) \times 10^8$	$0.97(\pm 0.02)$	$2.80(\pm 0.10)$
15 nm	$4.2(\pm 0.1) \times 10^{11}$	$2.0(\pm 0.2) \times 10^{11}$	$3.1(\pm 0.3) \times 10^9$	$1.05(\pm 0.07)$	$2.13(\pm 0.09)$

Te. Although WAL should induce a small enhancement to the conductivity at zero magnetic field<sup>8,17,18</sup>, its coexistence with a resistivity upturn (Fig. 2a) can be ascribed to the coexistence of WAL and EEI, as observed in other nanostructured systems (for example, see ref. 29). To gain further insights into the thickness-dependent evolution of WAL in Nb<sub>3</sub>SiTe<sub>6</sub> thin-flake crystals, we have fitted the magnetotransport data using the Hikami-Larkin-Nagaoka (HLN) model<sup>17,30</sup> (Fig. 3a) and extracted the characteristic quantum coherence and SOC fields,  $B_{\phi}$  and  $B_{SO}$ , respectively (Fig. 3b). At  $T = 2$  K, with increasing sample thickness from 6 to 15 nm,  $B_{SO}$  shows a very weak thickness dependence, whereas the value of  $B_{\phi}$  almost doubles (Fig. 3b), indicating that the enhanced WAL

signature in thin flakes is associated with better quantum coherence. This trend is best presented in terms of the dephasing time  $\tau_{\phi}$ , which has a more straightforward physical interpretation—it is the timescale over which the electron phase coherence is maintained. The dephasing time can be obtained from  $B_{\phi}$  via  $D\tau_{\phi} = \hbar/(4eB_{\phi})$  (refs 8,17,18), where  $D$  is the diffusion constant, which can be estimated from conductivity and density of states measurements (see further discussions in Methods). As shown in Fig. 3c, the dephasing rate  $\tau_{\phi}^{-1}$  increases by an order of magnitude with increasing thickness from 6 to 15 nm. The dephasing is expected to be stronger in even thicker flakes (for example,  $t = 30$  nm), in which the WAL signature disappears (Fig. 2b).

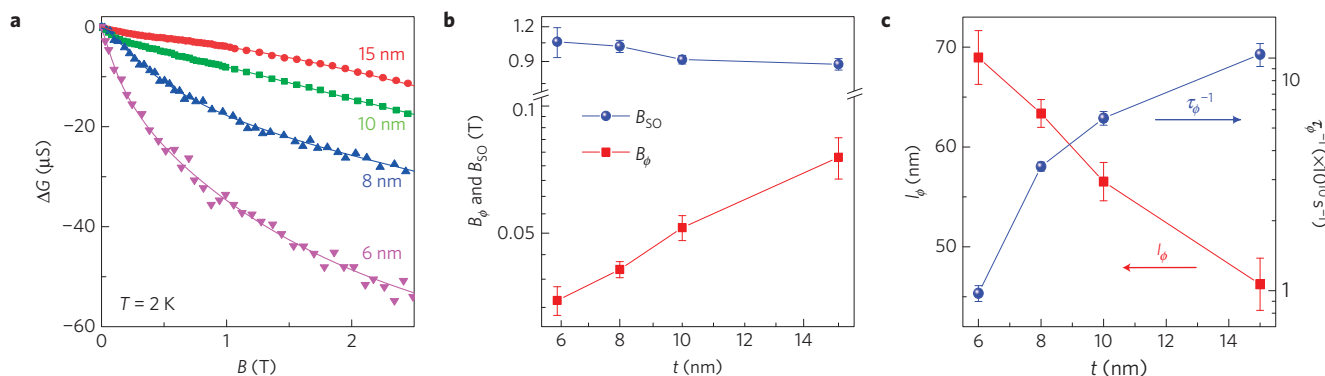


**Figure 3 | Analysis of WAL in  $\text{Nb}_3\text{SiTe}_6$  thin crystals.** **a**, Fits of the 2 K magnetotransport data of 8, 10 and 15 nm  $\text{Nb}_3\text{SiTe}_6$  thin-flake crystals to the 2D WAL model (HLN model). To perform the fit, the measured MR data is presented in the form of magnetoconductance  $\Delta G(B)$ . **b**, Characteristic fields  $B_{S0}$  and  $B_\phi$  at  $T=2$  K obtained from fitting the magnetoconductance to the 2D WAL model. **c**, Coherence length  $l_\phi$  and dephasing rate  $\tau_\phi^{-1}$  at  $T=2$  K extracted from the characteristic fields  $B_{S0}$  and  $B_\phi$ . The coherence length  $l_\phi$  [ $l_\phi^2 = D\tau_\phi = \hbar/(4e)B_\phi$ ] is larger than the flake thickness for all samples, confirming the validity of the 2D WAL model. Error bars in **b,c** are determined from the statistical errors of the fits of the magnetoconductance data to the HLN equation.

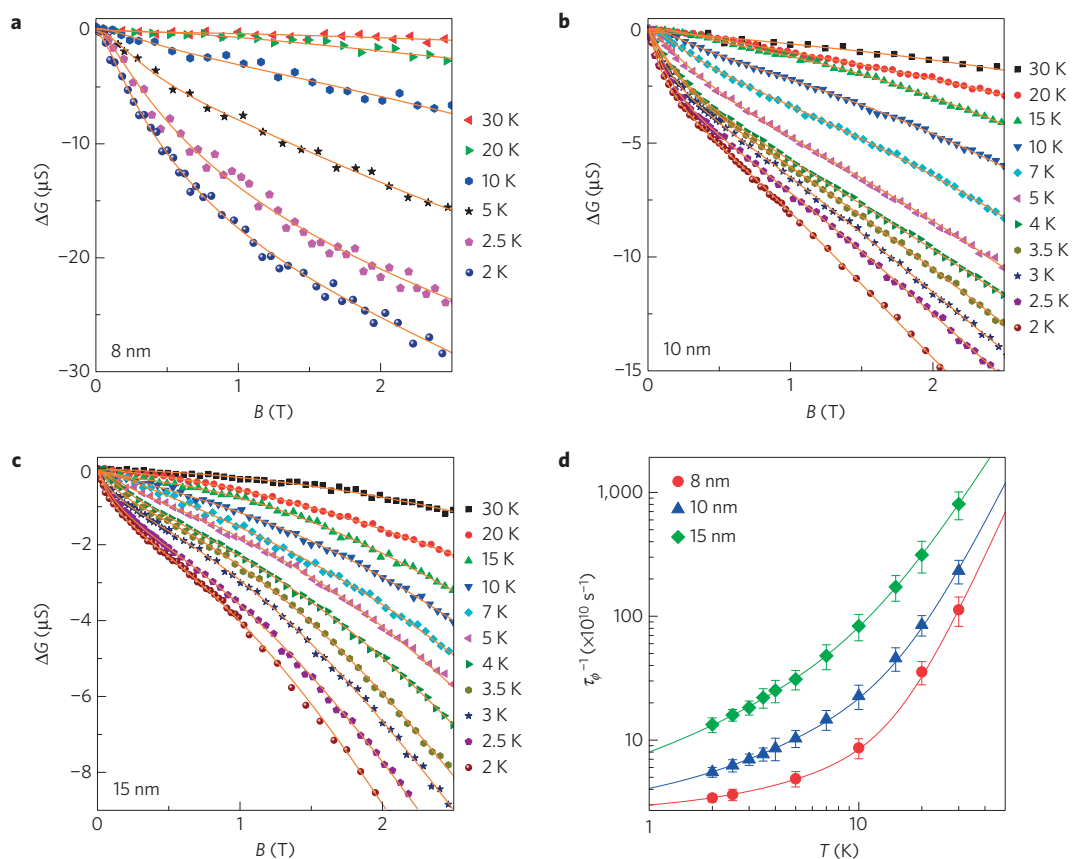


**Figure 4 | Thickness and temperature dependences of electron phase coherence in  $\text{Nb}_3\text{SiTe}_6$  thin crystals.** **a–c**, Fits of the magnetotransport data up to  $B=2.5$  T for 8 nm (**a**), 10 nm (**b**) and 15 nm (**c**)  $\text{Nb}_3\text{SiTe}_6$  thin-flake crystals to the 2D WAL model (HLN model). **d**, Temperature dependence of the dephasing rate  $\tau_\phi^{-1}$  for the 8, 10 and 15 nm samples, obtained from the fittings shown in **a–c**. Error bars represent uncertainties in the fits. The solid lines show the fits for the temperature dependence of  $\tau_\phi^{-1}$  (see text).

Generally, quantum coherence at low temperatures can be limited by a variety of inelastic scattering processes. Each of these processes contributes to phase decoherence, and the total dephasing rate can be approximated by the sum of the individual dephasing rates<sup>8</sup>. From the analyses shown below, we contend that the primary origin of the observed reduction in  $\tau_\phi^{-1}$  with decreasing flake thickness is the quantum confinement suppression of the inelastic e–ph scattering. The other primary scattering channels—such as

e–e, electron impurity and interfacial scattering—should all increase in dephasing rate with decreasing sample thickness<sup>31,32</sup>. Therefore, the fact that the total dephasing rate is suppressed as the system is brought closer to the 2D limit suggests that electron dephasing in our system is dominated by e–ph scattering.

The variation of e–ph interactions with sample thickness can be more fully investigated by measuring the temperature dependence of  $\tau_\phi^{-1}$ . Although e–e scattering dominates the dephasing process

at sub-kelvin temperatures, the contribution from e–ph interactions at a few kelvin is significant<sup>8,17</sup> and is clearly reflected in the temperature dependence of  $\tau_{\phi}^{-1}$  (for example, see ref. 8 and references therein). As shown in Fig. 4d,  $\tau_{\phi}^{-1}$  for 8, 10 and 15 nm samples can be described well by  $\tau_{\phi}^{-1} = \tau_0^{-1} + AT^{P_e} + BT^{P_{ph}}$ , where  $\tau_0^{-1}$  represents a residual zero temperature dephasing rate and  $AT^{P_e}$  and  $BT^{P_{ph}}$  are associated with e–e and e–ph inelastic scatterings, respectively<sup>8</sup>. The fittings of  $\tau_{\phi}^{-1}(T)$  yield  $P_e \sim 1$  for all samples (see Table 1), consistent with the prediction of the localization theory<sup>8</sup>. The value of  $P_{ph}$  decreases sharply from 3.63 for the 8 nm device to 2.13 for the 15 nm device. Although further theoretical work is needed to understand the underlying physics of these exponent values, the sharp changes of  $P_{ph}$  suggest the variation of e–ph interactions with the flake thickness. More importantly, the weight of e–ph interactions (that is, the prefactor  $B$ ) is reduced by almost three orders of magnitude in the 8 nm sample as compared with the 15 nm flake.

In lower dimensions, e–ph interactions can be modified by quantum confinement effects on the electronic band structure, as well as the phonon spectrum itself. As discussed in the Supplementary Information, the reduction of thickness leads to significant electronic band narrowing in a monolayer, which can, in principle, suppress e–ph interactions<sup>33</sup>. However, our band structure calculations did not show significant band narrowing in bilayer ( $t = 1.4$  nm) and thicker flakes. Therefore, the suppression of e–ph scattering in our samples cannot be attributed to 2D confinement on the electronic band structure. Instead, confinement should play a much more important role in its modification of the phonon spectrum, which in turn affects e–ph interactions. It has been proposed for decades that the 2D quantum confinement leads to enhanced e–ph interactions in free-standing films<sup>3,4,6</sup>, but suppresses e–ph interactions in ‘supported’ 2D systems with constrained boundaries<sup>6,7</sup>. Indeed, as we show in the Supplementary Information, the phonon wavelength estimated from both the experiments and *ab initio* calculations is  $\sim 80$ – $100$  nm at 2 K, which is much larger than the thickness of those devices exhibiting an enhanced WAL. This implies that the phonon spectrum develops a 2D character in our thin crystals.

The modification of e–ph interactions due to phonon dimensionality confinement has never been observed in WAL measurements<sup>19–21</sup>. Electron heating measurements have given mixed results as noted above. A major concern has been that the substrate modifies the phonon spectrum in ways that make the experimental results difficult to interpret<sup>8,17</sup>. However, both WAL (ref. 21) and electron heating<sup>16</sup> measurements have found that the temperature dependence of the e–ph scattering rate shows no marked difference between suspended and supported films, implying that substrate–film phonon coupling will not preclude the observation of phonon dimension crossover. We note all these previous studies were made on polycrystalline films, in which the e–ph interactions may be greatly affected by the limited mean free path<sup>22–24</sup> owing to significant grain boundary scattering. In contrast, our single-crystal nanoflakes should have minimal boundary scattering, resulting in the successful observation of enhanced electron coherence due to phonon dimension crossover. This highlights the advantage of using crystallized 2D materials to study electron transport in reduced dimensions.

## Methods

Methods and any associated references are available in the [online version of the paper](#).

Received 20 October 2014; accepted 31 March 2015;  
published online 4 May 2015

## References

- Novoselov, K. S. *et al.* Electric field effect in atomically thin carbon films. *Science* **306**, 666–669 (2004).
- Mak, K. F., Lee, C., Hone, J., Shan, J. & Heinz, T. F. Atomically thin MoS<sub>2</sub>: A new direct-gap semiconductor. *Phys. Rev. Lett.* **105**, 136805 (2010).
- Belitz, D. & Das Sarma, S. Inelastic phase-coherence time in thin metal films. *Phys. Rev. B* **36**, 7701–7704 (1987).
- Johnson, K., Wybourne, M. N. & Perrin, N. Acoustic-mode coupling and electron heating in thin metal films. *Phys. Rev. B* **50**, 2035–2038 (1994).
- Yu, S., Kim, K., Strosio, M. & Iafate, G. Electron–acoustic-phonon scattering rates in cylindrical quantum wires. *Phys. Rev. B* **51**, 4695–4698 (1995).
- Glavin, B. A., Pipa, V. I., Mitin, V. V. & Strosio, M. A. Relaxation of a two-dimensional electron gas in semiconductor thin films at low temperatures: Role of acoustic phonon confinement. *Phys. Rev. B* **65**, 205315 (2002).
- Tienda-Luna, I. M. *et al.* Effect of confined acoustic phonons on the electron mobility of rectangular nanowires. *Appl. Phys. Lett.* **103**, 163107 (2013).
- Lin, J. J. & Bird, J. P. Recent experimental studies of electron dephasing in metal and semiconductor mesoscopic structures. *J. Phys. Condens. Matter* **14**, R501 (2002).
- Perrin, N. Acoustic-phonon decoherence and electron transport in metallic nanostructures. *J. Phys. Condens. Matter* **19**, 216222 (2007).
- Seyler, J. & Wybourne, M. Acoustic waveguide modes observed in electrically heated metal wires. *Phys. Rev. Lett.* **69**, 1427–1430 (1992).
- Hone, J., Batlogg, B., Benes, Z., Johnson, A. T. & Fischer, J. E. Quantized phonon spectrum of single-wall carbon nanotubes. *Science* **289**, 1730–1733 (2000).
- Nabity, J. & Wybourne, M. Evidence for two-dimensional phonons in a thin metal film. *Phys. Rev. B* **44**, 8990–8996 (1991).
- Song, S.-H., Pan, W., Tsui, D. C., Xie, Y. H. & Monroe, D. Energy relaxation of two-dimensional carriers in strained Ge/Si<sub>0.4</sub>Ge<sub>0.6</sub> and Si/Si<sub>0.7</sub>Ge<sub>0.3</sub> quantum wells: Evidence for two-dimensional acoustic phonons. *Appl. Phys. Lett.* **70**, 3422–3424 (1997).
- Sugaya, T. *et al.* Electron–phonon scattering in an etched InGaAs quantum wire. *Physica B* **314**, 99–103 (2002).
- Karvonen, J. T. & Maasilta, I. J. Influence of phonon dimensionality on electron energy relaxation. *Phys. Rev. Lett.* **99**, 145503 (2007).
- DiTusa, J. E., Lin, K., Park, M., Isaacson, M. S. & Parpia, J. M. Role of phonon dimensionality on electron–phonon scattering rates. *Phys. Rev. Lett.* **68**, 1156–1159 (1992).
- Bergmann, G. Weak localization in thin films: A time-of-flight experiment with conduction electrons. *Phys. Rep.* **107**, 1–58 (1984).
- Lee, P. A. & Ramakrishnan, T. V. Disordered electronic systems. *Rev. Mod. Phys.* **57**, 287–337 (1985).
- Peters, R. P. & Bergmann, G. Dependence of the phase-coherence time in weak localization on electronic mean free path and film thickness. *J. Phys. Soc. Jpn* **54**, 3478–3487 (1985).
- Raffy, H., Nédellec, P., Dumoulin, L., MacLachlan, D. S. & Burger, J. P. Anomalous magnetoresistance in 2D Pd and PdHx films. *J. Phys.* **46**, 627–635 (1985).
- Kwong, Y. K., Lin, K., Isaacson, M. S. & Parpia, J. M. An attempt to observe phonon dimensionality crossover effects in the inelastic scattering rate of thin free-standing aluminum films. *J. Low Temp. Phys.* **88**, 261–272 (1992).
- Pippard, A. B. CXXII. Ultrasonic attenuation in metals. *Philos. Mag.* **46**, 1104–1114 (1955).
- Bergmann, G. Electron–electron interaction in superconductors with impurities. *Phys. Lett. A* **29**, 492–493 (1969).
- Sergeev, A. & Mitin, V. Electron–phonon interaction in disordered conductors: Static and vibrating scattering potentials. *Phys. Rev. B* **61**, 6041–6047 (2000).
- Li, J., Badding, M. E. & DiSalvo, F. J. Synthesis and structure of Nb<sub>3</sub>SiTe<sub>6</sub>, a new layered ternary niobium telluride compound. *J. Alloys Compd.* **184**, 257–263 (1992).
- Lee, C. *et al.* Anomalous lattice vibrations of single- and few-layer MoS<sub>2</sub>. *ACS Nano* **4**, 2695–2700 (2010).
- Efros, A. L. & Pollak, M. *Electron–Electron Interactions in Disordered Systems* (Elsevier, 1985).
- Andrei, N., Furuya, K. & Lowenstein, J. H. Solution of the Kondo problem. *Rev. Mod. Phys.* **55**, 331–402 (1983).
- Natelson, D., Willett, R. L., West, K. W. & Pfeiffer, L. N. Molecular-scale metal wires. *Solid State Commun.* **115**, 269–274 (2000).
- Hikami, S., Larkin, A. I. & Nagaoka, Y. Spin–orbit interaction and magnetoresistance in the two dimensional random system. *Progr. Theor. Exp. Phys.* **63**, 707–710 (1980).
- Altshuler, B. L., Aronov, A. G. & Lee, P. A. Interaction effects in disordered Fermi systems in two dimensions. *Phys. Rev. Lett.* **44**, 1288–1291 (1980).
- Li, S.-L. *et al.* Thickness-dependent interfacial Coulomb scattering in atomically thin field-effect transistors. *Nano Lett.* **13**, 3546–3552 (2013).
- Kibis, O. V. Suppression of electron–phonon interaction in narrow-band crystals. *Russ. Phys. J.* **40**, 780–783 (1997).

### Acknowledgements

The authors are grateful to J. DiTusa for informative discussions. The work at Tulane is supported by the US National Science Foundation under grant DMR-1205469 and the NSF EPSCoR Cooperative Agreement No. EPS-1003897, with additional support from the Louisiana Board of Regents. P.W.A. and T.J.L. acknowledge the support of the US Department of Energy, Office of Science, Basic Energy Sciences, under Award No. DE-FG02-07ER46420. L.Y.A. and P.B.S. acknowledge the support of the Russian Science Foundation (project #14-12-01217) and are grateful to the Joint Supercomputer Center of the Russian Academy of Sciences and 'Lomonosov' Research Computing Center for the opportunity of using a cluster computer for the quantum-chemical calculations. P.B.S. acknowledges a Grant of the President of the Russian Federation for government support of young PhD scientists MK-6218.2015.2 (project ID 14.Z56.15.6218-MK). Z.I.P. acknowledges the support of the Leading Science School program (No NSh-2886.2014.2). D.N. and H.J. acknowledge support through the US Department of Energy, Office of Science, Basic Energy Sciences award DE-FG02-06ER46337. The work at UNO is supported by the US National Science Foundation under the NSF EPSCoR Cooperative Agreement No. EPS-1003897, with additional support from the Louisiana Board of Regents.

### Author contributions

J.H., J.Y.L., H.W.Z. and Z.Q.M. carried out bulk sample growth and characterization, including XRD, resistivity and specific heat measurements. J.H., X.L., C.L.Y. and J.W. fabricated the nano-devices. J.H., X.L., T.J.L., P.W.A., S.M.A.R., and L.S. collected resistivity and magnetotransport data for the nano-devices. J.H. and J.B.H. carried out TEM measurements. H.J. and D.N. performed Raman spectrum measurements. L.Y.A., Z.I.P. and P.B.S. calculated the electronic structure. J.H., J.W., Z.Q.M., P.W.A., D.N. and P.B.S. analysed the data and wrote the manuscript. J.H. and X.L. contributed equally to this work. This project was supervised by Z.Q.M. and J.W.

### Additional information

Supplementary information is available in the [online version of the paper](#). Reprints and permissions information is available online at [www.nature.com/reprints](http://www.nature.com/reprints).

Correspondence and requests for materials should be addressed to J.W. or Z.Q.M.

### Competing financial interests

The authors declare no competing financial interests.

## Methods

**Bulk sample preparation and characterization.** The Nb<sub>3</sub>SiTe<sub>6</sub> bulk single crystals were synthesized with a stoichiometric mixture of starting elements using chemical vapour transport. During growth the temperature was set at 950 °C and 850 °C, respectively, for the hot and cold ends of the double zone tube furnace. Sheet-like single crystals with metal lustre (see inset of Fig. 1b) can be obtained at the cold zone after two weeks' growth.

The composition and structure of these single crystals were checked using energy-dispersive X-ray spectroscopy and X-ray diffraction measurements. The structure of Nb<sub>3</sub>SiTe<sub>6</sub> is similar to that of transition metal dichalcogenides MX<sub>2</sub> (for example, MoS<sub>2</sub>); both are formed from stacks of sandwich layers, with comparable van der Waals gaps. In MX<sub>2</sub>, each X–M–X sandwich layer is composed of edge-sharing trigonal MX<sub>6</sub> prisms (Supplementary Fig. 1c,d), whereas the Te–(Nb,Si)–Te sandwich layer of Nb<sub>3</sub>SiTe<sub>6</sub> consists of face- and edge-sharing NbTe<sub>6</sub> prisms, with Si ions inserting into interstitial sites among these prisms (Supplementary Fig. 1a,b).

**Nanoflake preparation and characterization.** To avoid any possible secondary phase in our single crystals, in addition to the careful characterization of bulk single crystals, we have used energy-dispersive X-ray spectroscopy to check tiny pieces of single crystal on the Scotch tapes used for exfoliation. The exfoliated Nb<sub>3</sub>SiTe<sub>6</sub> thin-flake crystals were characterized using Raman spectra measurements and transmission electron microscope (TEM) observations. Compared with MX<sub>2</sub>, which exhibits only E<sub>2g</sub><sup>1</sup> and A<sub>1g</sub> phonon modes<sup>26</sup>, Nb<sub>3</sub>SiTe<sub>6</sub> exhibits a greater number of Raman modes (Supplementary Fig. 2a), which may be attributed to its relatively complex lattice structure. Unfortunately, we were unable to identify these Raman modes owing to the lack of theoretical studies of those phonon spectra. However, we observed noticeable red- and blueshifts caused by decreasing flake thickness for the 165 and 225 cm<sup>-1</sup> modes, respectively (Fig. 1f). The phase and quality of Nb<sub>3</sub>SiTe<sub>6</sub> thin-flake crystals can be demonstrated by TEM observations. As shown in Supplementary Fig. 2b, all the [010]-zone electron diffraction spots can be indexed according to the crystal structure of Nb<sub>3</sub>SiTe<sub>6</sub>, consistent with excellent crystallinity. Moreover, the atomic resolution image shows no visible amorphous structure (Supplementary Fig. 2c) even after a few weeks' exposure to ambient environment, confirming the stability of the few-layer Nb<sub>3</sub>SiTe<sub>6</sub>.

The Nb<sub>3</sub>SiTe<sub>6</sub> nano-devices were fabricated on freshly cleaved single-crystal flakes using standard electron-beam lithography. Electrical contacts [Ti (5 nm)/Au (50 nm)] were thermally deposited on top of thin-flake crystals using the conventional lift-off technique. The device was then annealed at 200 °C in a vacuum tube furnace for 2 h to remove resist residue and reduce the contact resistance. The transport measurements for both bulk and nano crystals were performed in a physical properties measurement system (PPMS).

**Distinguishing between WAL and EEI contribution to MR.** The low-temperature resistivity upturns for all thin flakes follow a logarithmic temperature dependence, with some deviation for the thinnest (6 nm) sample (Supplementary Fig. 5). The log(*T*) dependence is a signature of 2D EEI or WL (refs 18,27), whereas the latter scenario can be excluded by the observation of positive MR (Fig. 2b,c). Indeed, the effect of EEI is expected to be more pronounced with reduced sample thickness<sup>18,29</sup>. The deviation from the log(*T*) dependence seen in the thinnest (6 nm) samples may be associated with the additional scattering mechanism (that is, interfacial scattering). 2D WAL also results in a log(*T*) dependence with opposite sign<sup>18</sup>. It is not surprising to observe EEI (leading to resistively upturns) and WAL (leading to reduced resistivity) in the same system given their different origin<sup>17,18</sup>. In fact, the coexistence of these two quantum phenomena has been observed in many other nanostructured systems<sup>29,34</sup>. Note that Kondo physics, another possible cause of a logarithmic correction to the resistivity at low temperatures, is eliminated as a contribution in this case because it would manifest as a striking deviation (one that we do not observe) in the expected temperature and field dependence of the WAL.

On the other hand, although both WAL (refs 8,17) and EEI (refs 18,27) have been suggested to share similar field dependences of MR—logarithmic and quadratic field dependences for strong and weak fields, respectively—their characteristic fields are distinct. The characteristic field of EEI, that is,  $B_{\text{EEI}} \sim k_{\text{B}} T / g \mu_{\text{B}}$  (where *g* is the Landau factor), is usually very large and can be reached only at very low temperatures (for example,  $B_{\text{EEI}} \sim 7.4\text{--}1.6$  T at *T* = 2 K if *g* is taken as 0.4–1.8 for Nb (refs 35,36)). However, the characteristic field of WAL, that is,  $B_{\phi} \sim hc / 2el_{\phi}$ , is much weaker than that of EEI in a similar temperature range (for example,  $B_{\phi} \sim 0.01\text{--}0.1$  T at 2 K for Nb<sub>3</sub>SiTe<sub>6</sub> flakes (see Fig. 3b)). As  $B_{\phi} \ll B_{\text{EEI}}$ , the MR of Nb<sub>3</sub>SiTe<sub>6</sub> is expected to show a rapid increase in the low-field range if WAL applies, which is consistent with our observations (Fig. 2b,c). Furthermore, given that WAL originates from quantum interference between a pair of time-reversed closed-loop backscattering electrons, a perpendicular magnetic field flux causes an additional phase for electron waves and consequently suppresses quantum interference<sup>8,17,18</sup>. Therefore, WAL is extremely sensitive to magnetic field orientation. In contrast, EEI-induced MR is insensitive to field orientation<sup>27,37</sup>. Therefore, despite the resistivity upturn at zero magnetic field suggesting the

presence of EEI, as discussed above, our observation of anisotropic MR at low field (Fig. 2d) implies that the low-field MR originates from WAL.

**Evaluation of the electron phase decoherence rate  $\tau_{\phi}^{-1}$ .** Given that both the dephasing field  $B_{\phi}$  and coherence length  $l_{\phi}$  depend on an additional parameter—the diffusion constant  $D [l_{\phi}^2 = D\tau_{\phi} = \hbar / (4eB_{\phi})]$ —the dephasing processes is better reflected by the dephasing rate  $\tau_{\phi}^{-1}$ , which can be derived from  $D\tau_{\phi} = \hbar / (4eB_{\phi})$ . The diffusion constant *D* can be obtained via the Einstein relation  $1/\rho = e^2 \cdot D \cdot \text{DOS}(E_{\text{F}})$ , whereas the density of states at the Fermi level  $\text{DOS}(E_{\text{F}})$  can be evaluated from the Sommerfeld coefficient  $\gamma = (\pi^2/3) \cdot \text{DOS}(E_{\text{F}}) \cdot k_{\text{B}}$  for a non-interacting system. For bulk Nb<sub>3</sub>SiTe<sub>6</sub>,  $\gamma$  extracted from the specific heat measurements is 9.7 mJ mol<sup>-1</sup> K<sup>-2</sup> (Supplementary Fig. 8b), or  $6.5 \times 10^{-5}$  J cm<sup>-3</sup> K<sup>-2</sup> when normalized to volume. This value yields the  $\text{DOS}(E_{\text{F}})$  as  $1.6 \times 10^{22}$  eV<sup>-1</sup> cm<sup>-3</sup>, consistent with the value  $1.9 \times 10^{22}$  eV<sup>-1</sup> cm<sup>-3</sup> obtained from our density functional calculations. When the thickness of the sample is decreased to be comparable to the Fermi wavelength ( $\sim 0.34$  nm), the significant modification of the electronic band structure (for example, see monolayer band structure in Supplementary Fig. 3c) changes the  $\text{DOS}(E_{\text{F}})$ . However, such band structure modifications become much weaker in a bilayer sample (*t* = 1.4 nm) and are negligible in our *t* = 6–15 nm samples. Furthermore, EEI also leads to a reduction of  $\text{DOS}(E_{\text{F}})$  and causes a resistivity upturn (Supplementary Fig. 5). However, such  $\text{DOS}(E_{\text{F}})$  corrections should be small in 8, 10 and 15 nm flakes given their tiny (less than a few percent) resistivity upturns, suggesting that  $\text{DOS}(E_{\text{F}})$  should remain roughly constant in these samples.

The diffusion constant *D* at *T* = 2 K obtained from the Einstein relation varies by 500% with increasing thickness from 6 to 15 nm (Supplementary Fig. 7). Such a significant variation apparently cannot be understood in terms of EEI corrections to the density of states (even for the 6 nm flake EEI leads to only a 16% resistivity upturn), but should be due to the stronger effect of interfacial scattering in thinner flakes. Although the diffusion constant can affect WAL through its impact on the coherence length [ $l_{\phi}^2 = D\tau_{\phi} = \hbar / (4eB_{\phi})$ ], the reduced *D* in thinner flakes causes reduced  $l_{\phi}$  (that is, enhanced  $B_{\phi}$ ) and thus is not in favour of the observed WAL enhancement. Therefore, the observation of reduced  $B_{\phi}$  (enhanced  $l_{\phi}$ ) in thinner flakes is due to the remarkably reduced dephasing rate  $\tau_{\phi}^{-1}$ , which compensates the reduced *D*, as shown in Fig. 3c.

**Evaluation of phonon dimensionality.** The dimensionality of phonons in thin flakes is determined by the characteristic length of the lattice vibrations (that is, the phonon wavelength  $\lambda_{\text{p}}$ ). 2D quantum confinement effects are expected to occur when  $\lambda_{\text{p}}$  along the direction perpendicular to the plane is much greater than the sample thickness. When *T* is much less than the Debye temperature  $\Theta_{\text{D}}$ , the phonon wavelength can be estimated as  $\lambda_{\text{p}} \sim hv_{\text{s}} / k_{\text{B}} T$ , where  $v_{\text{s}}$  is the speed of sound in the sample<sup>38</sup>. The value of  $v_{\text{s}}$ , although not yet experimentally determined, can be estimated using  $\Theta_{\text{D}}$ , given that  $\Theta_{\text{D}}$  corresponds to the minimum wavelength of the phonon ( $\lambda_{\text{min}} \sim hv_{\text{s}} / k_{\text{B}} \Theta_{\text{D}}$ ), which should be equivalent to the lattice parameter.

The Debye temperature  $\Theta_{\text{D}}$  can be obtained from the specific heat measurements on the Nb<sub>3</sub>SiTe<sub>6</sub> bulk single crystal. The specific heat *C* of Nb<sub>3</sub>SiTe<sub>6</sub> consists of electronic and phonon contributions. The electronic specific heat can be simply represented by  $\gamma T$  in non-magnetic Nb<sub>3</sub>SiTe<sub>6</sub>, whereas the phonon specific heat can be written as  $(12/5)\pi^4 NR (T/\Theta_{\text{D}})^3 = \beta T^3$  (when normalized to the molar specific heat) at sufficiently low temperatures ( $T \ll \Theta_{\text{D}}$ ), where *N* is the number of atoms in the formula and *R* is the gas constant. The low-temperature specific heat of Nb<sub>3</sub>SiTe<sub>6</sub> can be fitted well to  $C = \gamma T + \beta T^3$ , with  $\gamma \sim 9.70$  mJ mol<sup>-1</sup> K<sup>-2</sup> and  $\beta \sim 2.02$  mJ mol<sup>-1</sup> K<sup>-4</sup> (Supplementary Fig. 8b), yielding the Debye temperature  $\Theta_{\text{D}} \sim 213$  K. Given that the lattice parameter is of the order of 1 nm, the speed of sound is estimated to be  $\sim 4.8$  km s<sup>-1</sup> from  $\lambda_{\text{min}} \sim hv_{\text{s}} / k_{\text{B}} \Theta_{\text{D}} \sim 1$  nm, consistent with the sound speed of typical metals ( $\sim$  a few km s<sup>-1</sup>). The phonon wavelength at 2 K can be further estimated from  $hv_{\text{s}} / k_{\text{B}} T \sim 100$  nm, comparable to values obtained from *ab initio* calculations (see Supplementary Information). Such a value is much greater than the thickness of the Nb<sub>3</sub>SiTe<sub>6</sub> thin flakes used in the magnetoresistance measurements ( $\leq 15$  nm), indicating the 2D nature of the phonons in those Nb<sub>3</sub>SiTe<sub>6</sub> thin flakes.

## References

- Breznay, N. P. *et al.* Weak antilocalization and disorder-enhanced electron interactions in annealed films of the phase-change compound GeSb<sub>2</sub>Te<sub>4</sub>. *Phys. Rev. B* **86**, 205302 (2012).
- Balanda, A. *et al.* The *g*-factor of the 21/2+ state in <sup>91</sup>Nb. *Acta Phys. Pol. B* **8**, 147–152 (1977).
- Safa, B. The second spectrum of niobium: II. Accurate fine structure study of odd-parity levels. *Phys. Scr.* **87**, 035303 (2013).
- Maniyala, N. *et al.* Magnetoresistance from quantum interference effects in ferromagnets. *Nature* **404**, 581–584 (2000).
- Giazotto, F., Heikkilä, T. T., Luukanen, A., Savin, A. M. & Pekola, J. P. Opportunities for mesoscopics in thermometry and refrigeration: Physics and applications. *Rev. Mod. Phys.* **78**, 217–274 (2006).